

Environmental Dependence of Star Formation in 9 EDisCS Galaxy Clusters

©2022

Justin Mann

B.A. Physics, University of Missouri Kansas City, 2012

B.A. Mathematics, University of Missouri Kansas City 2012

Submitted to the graduate degree program in Department of Physics and Astronomy and the Graduate Faculty of the University of Kansas in partial fulfillment of the requirements for the degree of Master of Science.

Dr. Gregory Rudnick, Chairperson

Committee members

Dr. Ian Crossfield

Dr. Hume Feldman

Date defended: July 22, 2022

The Thesis Committee for Justin Mann certifies
that this is the approved version of the following thesis :

Environmental Dependence of Star Formation in 9 EDisCS Galaxy Clusters

Dr. Gregory Rudnick, Chairperson

Date approved: July 22, 2022

Abstract

To understand the physical processes that govern the suppression of star formation in galaxies residing in over dense environments, it is necessary to track their journey into those regions. We present Multiband Imaging Photometer on Spitzer (MIPS) $24\mu m$ data covering the infall regions of 9 clusters chosen from the European Southern Observatory (ESO) Distant Cluster Survey (EDisCS) at intermediate redshifts ($0.5 < z < 0.8$). In addition to the data obtained for the central cluster regions by the EDisCS survey, several spectroscopic surveys were performed and used to define cluster infall region membership. Using the $24\mu m$ flux as a proxy for dust obscured star formation rate (SFR), we find that the nominal fraction of infrared luminous galaxies within the cluster only reaches that of the field well beyond R_{200} . Furthermore, average star formation rates of cluster members show no trend with clustercentric radius, remaining consistent with the average field value throughout the cluster.

Contents

1	Introduction	1
2	Data	4
2.1	EDisCS	4
2.2	Follow-up Spectroscopy	5
2.2.1	LDP Spectra	6
2.2.2	Hectospec	7
2.3	UKIRT K-band Photometry	9
2.4	Infrared MIPS Data	9
2.4.1	Acquisition and Reduction	10
2.4.2	Photometry	13
2.4.3	Conversion to Star Formation Rate	14
2.4.4	MIPS Stacking	15
2.5	Sample Selection	16
2.5.1	Stellar Mass and Completeness	17
2.5.2	Defining Cluster Membership	19
2.5.3	Aggregate Cluster Sample	19
2.5.4	Defining Field Sample	20
3	Results	22
3.1	Star Forming Fraction	22
3.2	Average Star Formation	23
4	Discussion	26

5	Summary	27
6	Appendix	31

List of Figures

2.1	Histograms showing the three redshift sources for this work. The original FORS measured redshifts on top and the two new spectroscopic programs, Hectospec and LDP, in the middle and bottom panels respectively.	5
2.2	Redshift solutions derived from the Low Dispersion Prism program and photometric redshifts are compared to spectroscopic redshifts from FORS. The tighter correlation between the LDP and FORS redshifts illustrates why photometric redshifts are not used in our analysis of our cluster infall regions.	6
2.3	This is an example of a reduced and extracted Hectospec spectrum. Black is the observed flux vs. wavelength, blue is the noise spectrum, red lines are common emission lines redshifted to the HSRed solution wavelength. Visualizations such as this were used to verify the output of the HSRed pipeline for all target galaxies. .	8
2.4	Illustration of data coverage. Black dots are all galaxies with LDP redshifts, Red (passive) and Blue (star-forming) filled circles are all cluster members. R_{200} is shown as the black circle and the dashed square is the original coverage of EDisCS. The MIPS coverage of this particular cluster is shown as the shaded region that crosses over the general LDP field of view. Similar plots for all clusters can be found on the last pages.	10
2.5	This is an example of a full MIPS $24\mu m$ mosaic. The data were reduced and the mosaic was created with the MOPEX reduction package. Photometry on the MIPS images was done with the APEX package.	12

2.6 The left is an example of the WFI photometry. This is a smoothed r band image of the central cluster with red circles highlighting spectroscopically confirmed members. On the right is a zoom in of the MIPS $24\mu m$ data for the same field of view. Red circles again identify the location of cluster members and infall region galaxies. The slight rotation here is due to plotting in pixel space of the MIPS image which is a strip that does not line up with the RA or DEC axis. The large amount of membership locations that do not correspond with direct MIPS detections will be stacked later on in an attempt to characterize the average SFR of galaxies in our fields that are below the nominal flux/SFR limit in our study. 13

2.7 This is a plot of the rest frame U-V, V-J colors. The upper left hand corner defines the subset of galaxies deemed as passive to be excluded from the MIPS stacking exercise. Open circles are everything with UVJ colors in the redshift range $0.5 \leq z \leq 0.8$. Blue and red filled circles are mass complete cluster members above and below the SFR limit respectively. 16

2.8 The blue and red points show the M/L_V ratio vs $U - V$ color relationship for 6 exponentially decaying star formation histories ($t_0 = [1, 2, 4, 6, 8, 10]$) produced by EZGal with Chabrier IMFs and Bruzual Charlot SPS models. The red points are created by adding an attenuation factor of 1 to the V-band magnitudes. Ages of the stellar populations are limited to $7Gyr$ 17

2.9 MIPS derived SFRs vs $\log_{10}(M_*)$. Grey points are all galaxies in the sample within a range of $0.5 < z < 0.8$ with a mass and SFR measurement. Blue stars are spectroscopic cluster member galaxies with MIPS detections. The grey horizontal dashed line indicates the SFR limit. The dash-dot and solid vertical lines demark the mass limits for star forming and passive galaxies respectively. The shaded grey region is the star forming main sequence as measured in Whitaker et al. (2012). . . 18

2.10	The cumulative distributions of the field (green points), the clusters (blue points), and the redshift/stellar mass matched field (red points). The redshift and mass distributions of the field were simultaneously matched to those of the clusters. . . .	21
3.1	The histogram on top shows bin totals in red and SF totals in blue. These totals are summed over all clusters with galaxies above the mass complete limit. The lower panel shows fractions of SF galaxies in bins of R_{200} as the black points. Binomial limits for the SF fractions are given for each radial bin. Red points are the fractions calculated in two course bins, inside and outside of $2R_{200}$. Grey points are the star forming fractions from Finn et al. (2010) calculated with the mass and SFR limits from this study applied.	23
3.2	These are histograms of the SFR measured from 500 bootstrap iterations of the MIPS stack for each radial bin of our composite cluster. The solid black line is the SFR measure from the original stack and the dashed black lines indicate the 95 percentile region of the bootstrap iterations.	24
3.3	Average SFRs measured from stacked MIPS images of UVJ selected star forming galaxies. Error bars derived from the 95 percentile of 500 bootstrap iterations of each stack. Black cross hairs indicate cluster members with the specified radial bin. Gray bar represents the average SFR of field galaxies.	25

List of Tables

1.1	EDisCS Clusters	3
2.1	MIPS $24\mu m$ Scans	14
2.2	MIPS derived Limits	15

Chapter 1

Introduction

The field of galaxy evolution involves study of all the different mechanisms by which a galaxy can change its total mass, structure, and content. This work focuses on how large scale environment can enhance or hinder a galaxy's ability to form stars. To do this, we will utilize broadband photometry to separate passive and star-forming galaxies, infrared data to measure star formation rates (SFRs), and spectroscopy to separate field from cluster members. We will emphasize the role of external modes of star formation suppression within galaxies by analyzing any trends of star formation and passivity with the surrounding environment.

While it is important to understand how stellar mass (M_*) increases in the universe, it is equally important to understand the mechanisms by which star formation can be suppressed. The literature has formed a general consensus that both intrinsic and extrinsic mechanisms are contributing to the suppression of star formation over time (Peng et al., 2010), but the relative contributions of these mechanisms have yet to be determined.

Suppression mechanisms intrinsic to a galaxy regardless of the larger environment it occupies include supernova feedback, stellar winds, and AGN activity. These feedback mechanisms add energy to the interstellar medium, which can hinder the cooling process necessary for future star formation or expel the gas from the galaxy entirely.

A galaxy's star formation can also be suppressed by mechanisms that are completely dependent on factors external to the galaxy. Many studies have shown a discrepancy between the fraction of passive galaxies within over dense regions (groups and clusters) and those in less dense regions (the field). Higher passive fractions in clusters compared with the field (Balogh et al., 1998; Hogg et al., 2004; Kauffmann et al., 2004; Poggianti et al., 2006; McGee et al., 2009; Peng et al., 2010; Finn

et al., 2010) suggests that environmental effects within over dense regions are supplementing the suppression of star formation from intrinsic modes that are, perhaps, ever present. Such extrinsic modes of suppressing star formation abound and include ram pressure stripping (Gunn & Gott, 1972), harassment (Moore et al., 1996), strangulation (Larson et al., 1980), and even mergers that can ignite starburst (Hernquist & Mihos, 1995) which subsequently consumes much of the available gas and is followed by feedback mechanisms that prevent gas from cooling in the future. This work will focus on extrinsic modes of star formation suppression.

In order to measure star formation, it is necessary to trace the presence of young massive stars. When star formation occurs, these young stars are generally accompanied by large clouds of dust that can absorb ultraviolet (UV) light coming from the newly formed O and B stars and reradiate that light in the infrared (IR). Therefore, a firm grasp on the total IR luminosity of a galaxy can be used as a proxy for the presence of young massive stars and, hence, an instantaneous SFR. Direct measurements of young massive stars like H_α or the total ultraviolet luminosity, L_{UV} , do not account for star formation that is completely enshrouded by dust. Several studies (Puget et al., 1996; Dwek & Arendt, 1998; Fixsen et al., 1998; Hauser et al., 1998; Schlegel et al., 1998; Lagache et al., 1999; Gorjian et al., 2000; Wright & Reese, 2000; Wright, 2001) have suggested that as much as 50% of the optical/UV output of SF galaxies can be absorbed and reradiated in the IR. The fact that dust obscured star formation increases by about 2 orders of magnitude between $z \sim 0-2$ (Chary & Elbaz, 2001) also highlights the importance of measuring the mid IR emission of our sample (given the redshift range of $0.5 < z < 0.8$).

Furthermore, galaxy clusters and their surrounding regions serve as an excellent place to study extrinsic quenching, because it has been shown that the passive fraction of galaxies within clusters is significantly higher than that of the field (Hashimoto et al., 1998; Lewis et al., 2002; Gómez et al., 2003; Balogh et al., 2004; Kauffmann et al., 2004; Blanton & Moustakas, 2009). The fact that the passive fraction of galaxies increases with density on any scale, one must look at the entire spectrum of density regimes in order to capture the transition between what are nominal field values and those of the most dense central cluster regions.

Table 1.1: EDisCS Clusters

$ID_{cluster}$ (a)	$z_{cluster}$ (b)	$\sigma[\frac{km}{s}]$ (c)	R_{200} (d)	N_{field} (e)	$N_{members}$ (f)	$N_{MIPSmembers}$ (g)
cl1040.7-1155	0.7043	$418^{55.0}_{-46}$	0.70	106	26	7
cl1054.4-1146	0.6972	$589^{78.0}_{-70}$	0.99	75	30	11
cl1054.7-1245	0.7498	$504^{113.0}_{-65}$	0.82	200	71	25
cl1216.8-1201	0.7943	$1018^{73.0}_{-77}$	1.61	239	54	19
cl1232.5-1250	0.5414	$1080^{119.0}_{-89}$	1.99	187	72	10
cl1227.9-1138	0.6357	$574^{72.0}_{-75}$	1.00	222	19	2
cl1227.9-1138a	0.5826	$341^{42.0}_{-46}$	0.61	129	24	6
cl1354.2-1230	0.762	$648^{105.0}_{-110}$	1.05	189	31	14
cl1354.2-1230a	0.5952	$433^{95.0}_{-104}$	0.77	132	35	12

(a) The EDisCS cluster designation. (b) Cluster redshift obtained with FORS2 data. (c) Velocity Dispersion of the cluster. (d) The radius at which the density inside is 200 times the critical density of the universe. (e) The number of field galaxies selected from different pointings at the cluster redshift. (f) Number of cluster members. Members defined to be within 0.02 of the cluster redshift. (g) Number of cluster members with a $S/N > 3$ on the MIPS image at the r_{band} source locations.

This work intends to do just that by examining the infall regions of 9 clusters (See Table 1.1) between $0.5 < z < 0.8$ from the ESO Distant Cluster Survey (EDisCS, P.I. Simon D.M. White, LP 166.A-0162). By examining the spatial distribution of SF galaxies as far as $6R_{200}$ from the center of each cluster, we aim to sample the entire spectrum of density regimes that galaxies are known to inhabit.

The progression of this paper is as follows. §2.1 will outline the original EDisCS data, while §2.2 will introduce two follow up spectroscopic surveys used in this work. The MIPS $24\mu m$ data is presented with an overview of the reduction process in §2.4. The definitions of our cluster and field samples are given in §2.5. Finally, §3 will outline our results.

Chapter 2

Data

In this section, we will outline the original data presented by the EDisCS used in this work, along with ancillary data obtained for the current project. The latter includes two new spectroscopic surveys using the Low Dispersion Prism (LDP) on Magellan and Hectospec on the MMT, additional K -band photometry from UKIRT, and mid-infrared measurements from the Multiband Imaging Photometer (MIPS) aboard the Spitzer Space Telescope. The larger spatial extent of the new MIPS data and spectroscopic programs relative to the original EDisCS allow for the inspection of the infall regions surrounding the original clusters.

2.1 EDisCS

This work is built on the foundation of the ESO Distant Cluster Survey (EDisCS). A full description of the initial survey is given in White et al. (2005) and a brief overview is given here. Candidate clusters were chosen as 5σ detections from the Las Campanas Distant Cluster Survey of Gonzalez et al. (2001). Follow up confirmation and subsequent deep broadband photometry (BVRI) taken with FORS2 on VLT paved the way for optical spectroscopy performed with the same instrument. J and K -band photometry was taken with NTT/SOFI. The photometry and medium resolution spectroscopy from FORS on the VLT covered only the central regions of the clusters. The relevant clusters to this work, a subset of 9 that have wide field MIPS $24\mu m$ data, contain FORS2 spectra only for galaxies within $\sim \frac{1}{2}R_{virial}$ of the brightest cluster galaxy (BCG). Galaxy mass estimates are provided in Vulcani et al. (2010) using mass to light ratios based on Bell & de Jong (2001). Total dynamical masses of the clusters are also estimated from weak lensing measurements presented in

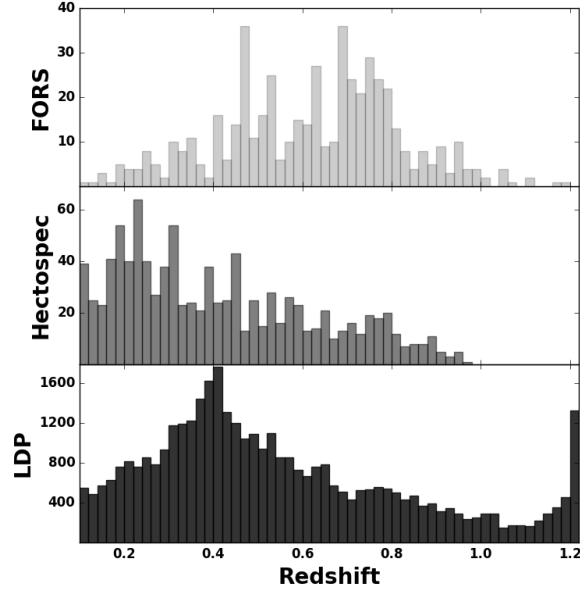


Figure 2.1: Histograms showing the three redshift sources for this work. The original FORS measured redshifts on top and the two new spectroscopic programs, Hectospec and LDP, in the middle and bottom panels respectively.

Clowe et al. (2006).

A plethora of ancillary data have also been added to the original EDisCS. Among these are mid Infrared measurements from MIPS $24\mu m$ introduced by Finn et al. (2010) and the current work, and wide field low resolution spectroscopy taken with the Low Dispersion Prism (LDP) for IMACS on Magellan (Just et al. (2019)).

2.2 Follow-up Spectroscopy

The necessity to extend the spatial extent of the EDisCS investigation of SFR as a function of cluster-centric radius has prompted several follow up spectroscopic surveys. The large spatial extent of the infall regions warrants the use of exposure time efficient spectroscopy. The spectroscopic programs described in the following sections serve to facilitate the assessment of cluster/infall-region membership and distinguish those members from fore/background galaxies. Histograms of the redshifts derived from our 3 spectroscopic programs are shown in Figure 2.1.

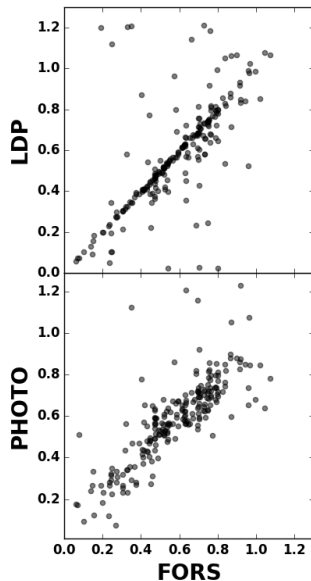


Figure 2.2: Redshift solutions derived from the Low Dispersion Prism program and photometric redshifts are compared to spectroscopic redshifts from FORS. The tighter correlation between the LDP and FORS redshifts illustrates why photometric redshifts are not used in our analysis of our cluster infall regions.

2.2.1 LDP Spectra

The Low Dispersion Prism (LDP) spectra from IMACS on Magellan allowed for just such an economic survey to be performed. Our LDP program (Just et al., 2019) yielded just over 20,000 redshifts. This addition accounts for 2,682 new cluster members to the original EDisCS sample and allows for the creation of a field sample from within our own data by compiling all galaxies within our redshift range that are not flagged as members. The added cluster members also increase the spatial extent of our study out to at least $6R_{200}$ for all the clusters. Despite the low resolution of this data, $\frac{\lambda}{\Delta\lambda} \sim 20-120$, redshifts inferred from them are quite accurate when compared with redshifts calculated using FORS spectra. Figure 2.2 illustrates this point by plotting z_{FORS} vs z_{LDP} for all galaxies that have coverage from both surveys. The time-cost efficiency of the LDP survey sacrificed little by way of the redshift estimations and is clearly more precise than other time efficient redshift estimation methods (ie, the photometric redshifts which are also plotted against the FORS redshifts in the bottom panel of Figure 2.2).

2.2.2 Hectospec

Another follow up survey with the Hectospec multifiber spectrograph on the MMT 6.5m, proposal ID: 2013a-UAO-S1B, targeted galaxies within our clusters that had no previous spectroscopy and gave first priority to star formers (SFRs being based on a preliminary analysis of the MIPS $24\mu\text{m}$ data done by Finn et al. (2010)). Hectospec produces 300 fiber fed spectra per 1° pointing (Fabricant et al., 2005) with a resolution of ~ 1.2 /pixel over the range of 3650 – 9200. In total, 1604 spectra were reduced and extracted with the HSRed package developed by Richard Cool (Papovich et al., 2006). Quality of redshift solution flags are given as an output from the HSRed code, but these were not believed blindly. Papovich et al. (2006) found that 5% of their redshift solutions from the automated HSRed package were wrong and had to be corrected by hand where possible.

All redshift solutions in the current work were visually inspected by redshifting common emission/absorption lines associated with recent star formation to the wavelength given by the redshift solution and over plotting them on the observed spectra (see Figure 2.3). Visual inspection of even the high quality flagged solutions was necessary because the redshift calculating algorithm involves linear combinations of 4 template spectra and noisy measured spectra can sometimes have multiple redshifts solutions that give similar quality fits to the data. Of all the solutions inspected, 1191 redshifts calculated with HSRed were deemed to be trustworthy (a 74% success rate). This added 59 members to our clusters and 568 more galaxies to our field sample.

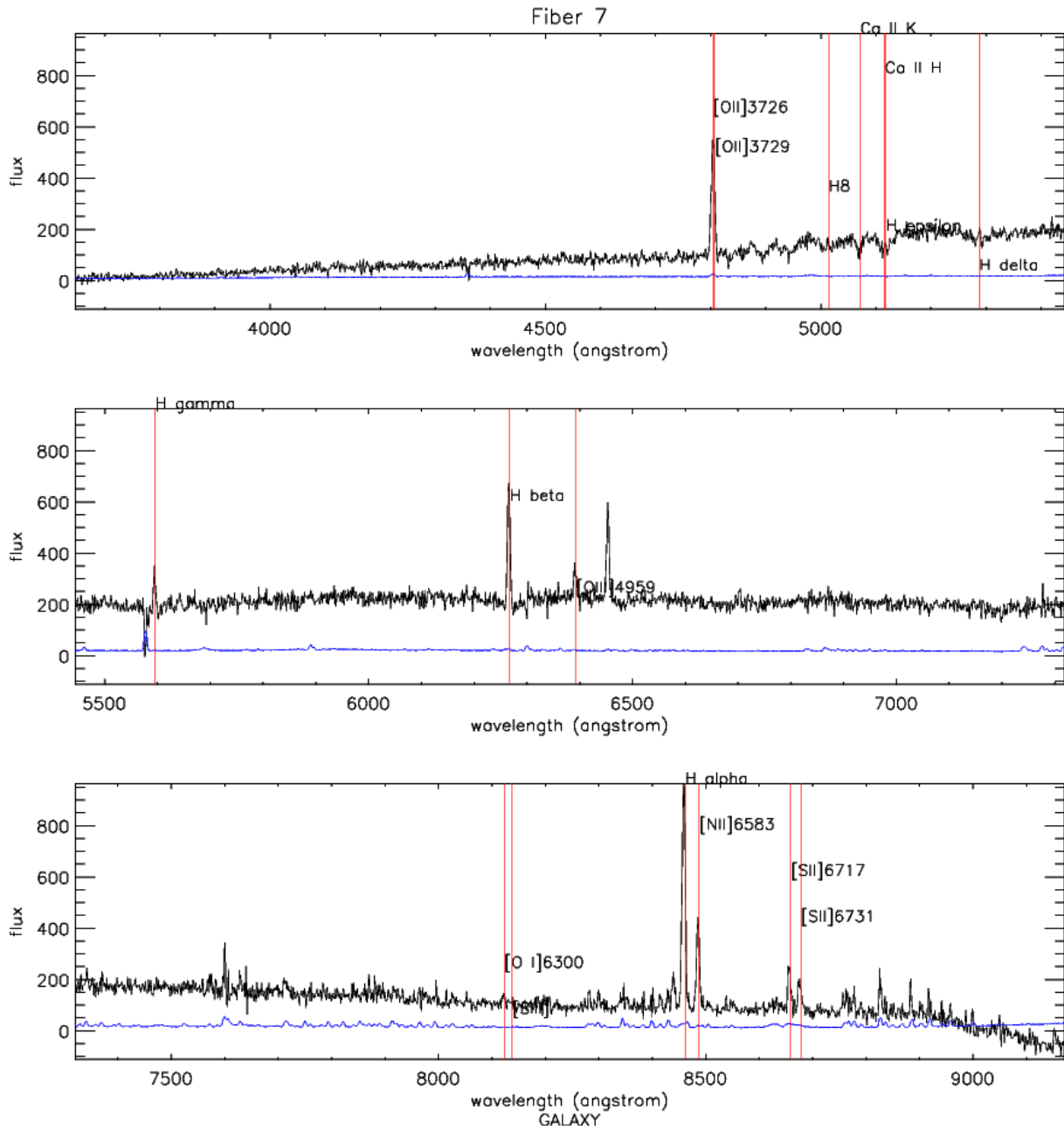


Figure 2.3: This is an example of a reduced and extracted Hectospec spectrum. Black is the observed flux vs. wavelength, blue is the noise spectrum, red lines are common emission lines redshifted to the HSR solution wavelength. Visualizations such as this were used to verify the output of the HSR pipeline for all target galaxies.

2.3 UKIRT K-band Photometry

In order to reliably classify star-forming versus passive galaxies with the standard UVJ diagram diagnostics, K -band photometry is required. In the redshift range of the EDisCS clusters, observed K -band closely approximates the rest-frame J -band, giving us a more reliable anchor point during the SED fitting portion of the rest-frame color calculations. Not all clusters were observed in the K -band with the original NEWFIRM survey, hence, follow up observations were required.

We obtain additional K -band data with the UKIRT wide field camera and reduce them with standard packages provided by UKIRT (Currie et al. (2014)). The default flatfield image provided in the standard reduction package was insufficient for our particular case. Large scale gradients were detected after flatfielding with the provided image, necessitating the need to construct an original flatfield image from our own data. Flatfielding and sky subtraction were performed on the Basic Calibrated Data (BCDs) that we subsequently stitched together to produce a $\sim 15900 \times 15900$ pixel mosaic of each field. After convolving the K -band image to match the seeing of the original R -band images, we use SExtractor running in dual image mode to measure the K -band flux at each R -band detection location.

2.4 Infrared MIPS Data

In order to extend the discussion of star-forming fractions to cluster infall regions, we obtained additional MIPS $24\mu m$ scan mode (Rieke et al., 2004) data for eight EDisCS fields of view. See Figure 2.4 for an illustration of the MIPS coverage. This sample ranks among the largest wide field $24\mu m$ surveys to date (see Lonsdale et al. (2003) for another large scale IR survey). Though not as deep as the original $24\mu m$ data presented in Finn et al. (2010), we are able to distinguish total L_{IR} down to $\sim 1.4 \times 10^{11} L_{\odot}$ which corresponds to star formation rates of $\sim 20 M_{\odot}/year$. The throughput curve of the MIPS $24\mu m$ channel spans a range of $\sim 20 - 30\mu m$ which corresponds to an observed range of $\sim 12 - 18\mu m$ at our mean redshift of $z \sim 0.6$.

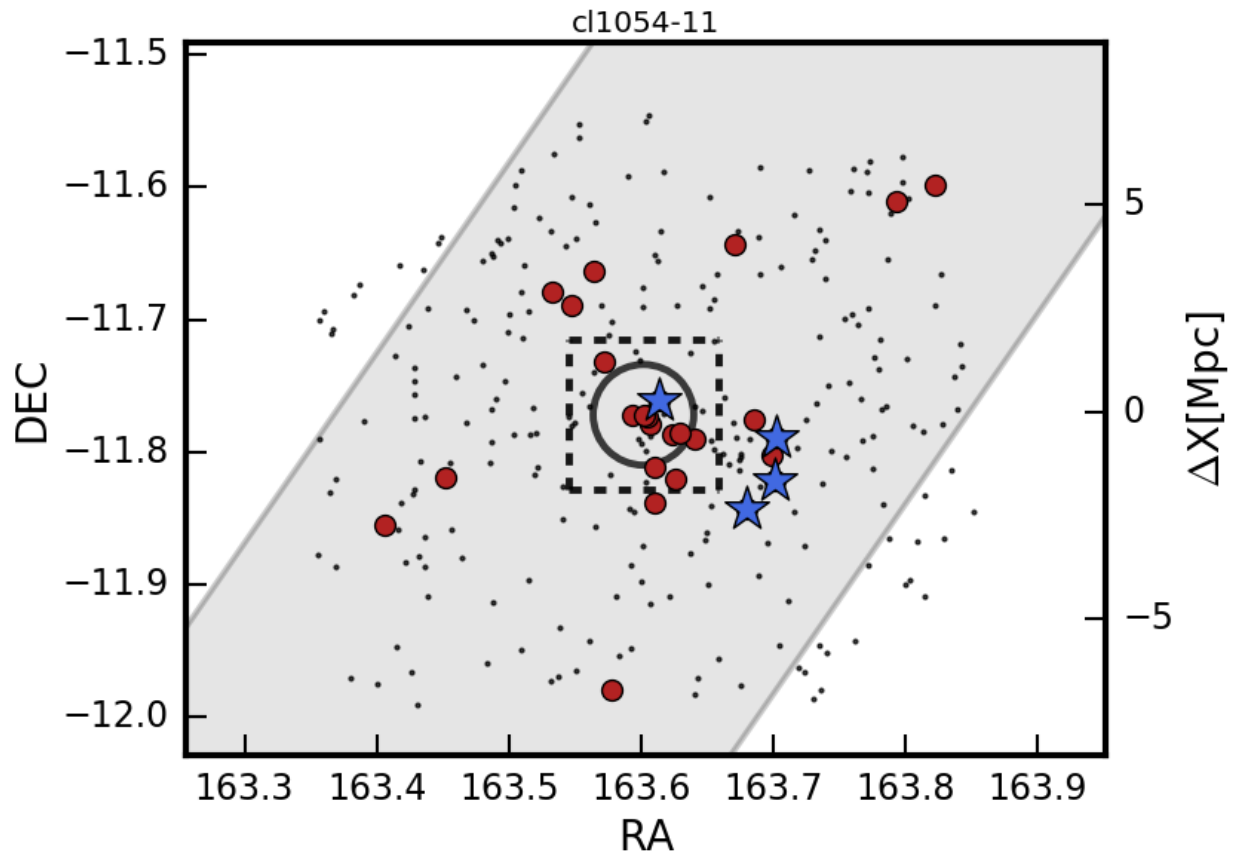


Figure 2.4: Illustration of data coverage. Black dots are all galaxies with LDP redshifts, Red (passive) and Blue (star-forming) filled circles are all cluster members. R_{200} is shown as the black circle and the dashed square is the original coverage of EDisCS. The MIPS coverage of this particular cluster is shown as the shaded region that crosses over the general LDP field of view. Similar plots for all clusters can be found on the last pages.

2.4.1 Acquisition and Reduction

The EDisCS collaboration obtained 16 scan mode Multiband Imaging Photometer on Spitzer (MIPS) data collections, resulting in mosaics of 11 clusters (Program ID: *EDISCSWF/20389* and Program ID: *GRU_EDISCSWIDE/50733* in the years 2006 and 2009 respectively). The images have a mean flux limit of $\sim 300 \mu\text{Jy}/\text{sr}$ which translates to a mean total L_{IR} of $2 \times 10^{11} L_{\odot}$ with a standard deviation of $3 \times 10^6 L_{\odot}$. I reduced the data with the MOPEX package provided by NASA/IPAC following prescriptions described at <http://irsa.ipac.caltech.edu>. The scan mode of MIPS produces thousands of basic-calibration-data (BCD) images which are reduced individually

and subsequently stitched together to form one mosaic per field of view. The first step in reducing the BCD images is flatfielding of the individual frames. After an initial source detection and masking of these sources is done, the median background is measured and subtracted from each masked frame, leaving only artifacts to be removed. I flatfielded the individual BCD images using a stack of the artifact images and these flatfielded BCDs were then used to make the final mosaic image. A full MIPS mosaic is shown in Figure 2.5 and a zoom in of one of these mosaics is given in Figure 2.6 alongside the corresponding *R*-band image from the wide field imager (WFI) on the ESO/MPG 2.2m telescope in La Silla. These images are a zoom in of the central cluster and the lack of MIPS flux at *R*-band source locations motivates the use of forced photometry on the MIPS images at these locations.

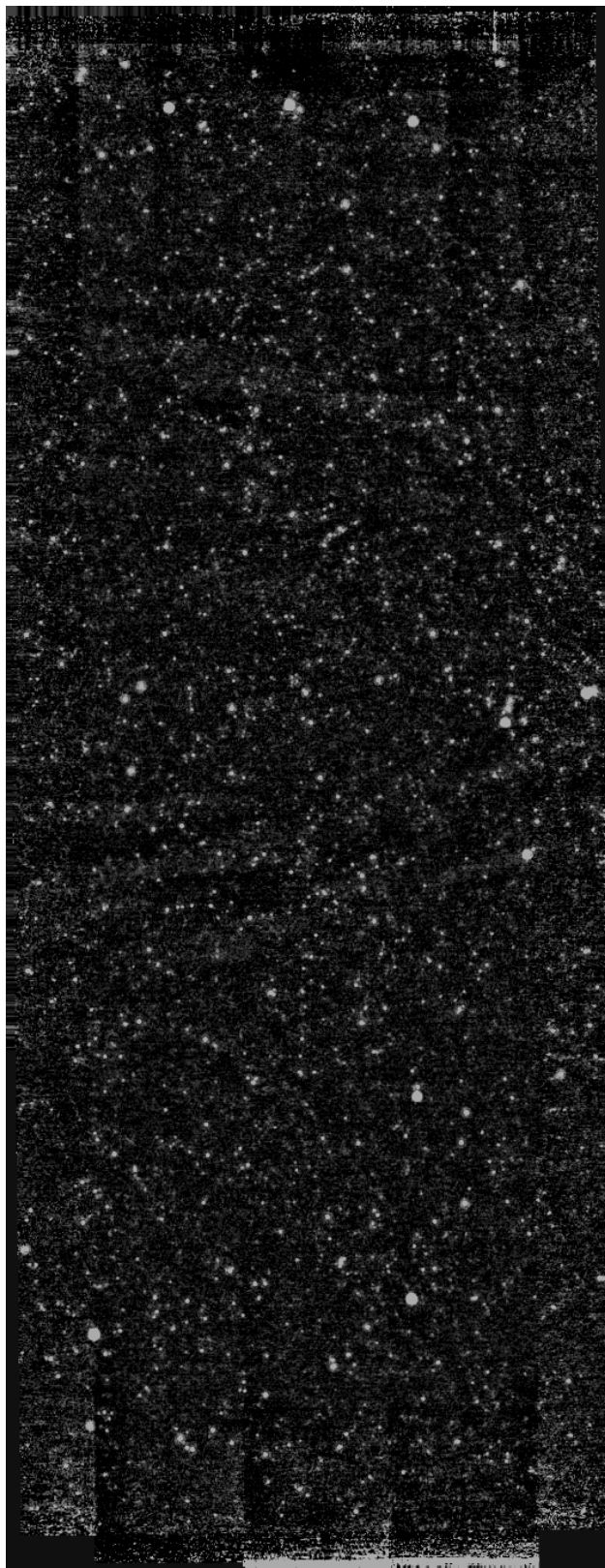


Figure 2.5: This is an example of a full MIPS $24\mu m$ mosaic. The data were reduced and the mosaic was created with the MOPEX reduction package. Photometry on the MIPS images was done with the APEX package.

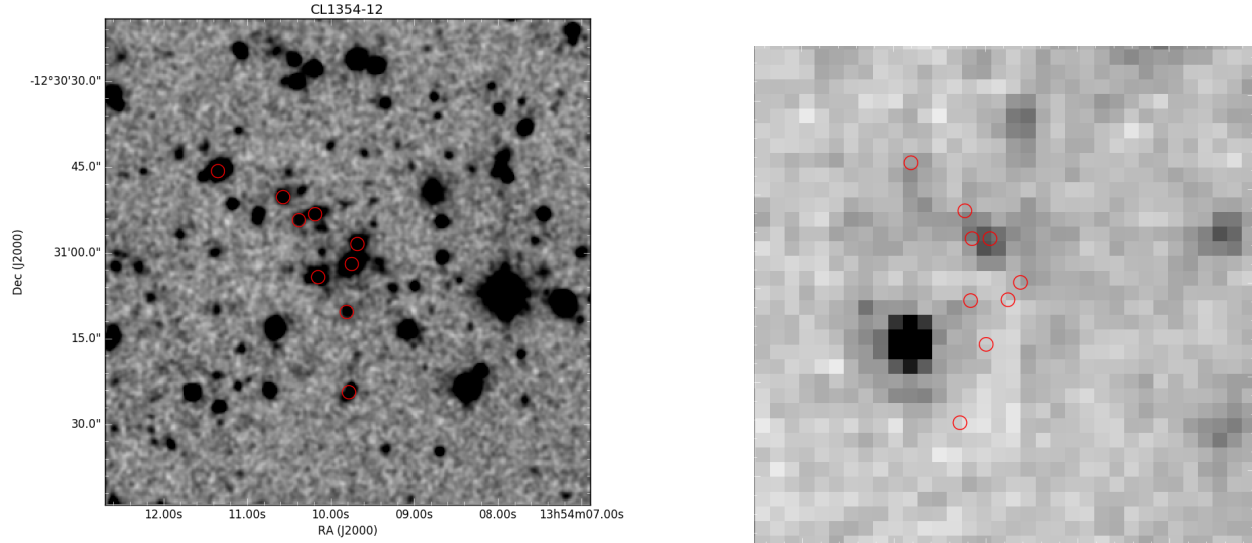


Figure 2.6: The left is an example of the WFI photometry. This is a smoothed r band image of the central cluster with red circles highlighting spectroscopically confirmed members. On the right is a zoom in of the MIPS $24\mu\text{m}$ data for the same field of view. Red circles again identify the location of cluster members and infall region galaxies. The slight rotation here is due to plotting in pixel space of the MIPS image which is a strip that does not line up with the RA or DEC axis. The large amount of membership locations that do not correspond with direct MIPS detections will be stacked later on in an attempt to characterize the average SFR of galaxies in our fields that are below the nominal flux/SFR limit in our study.

2.4.2 Photometry

The reduction package MOPEX also comes with a photometry analyzing package called APEX. This, more or less, is a specialized version of SExtractor that has been modified to handle IR data (specifically Spitzer data) more robustly. An initial step in measuring the MIPS flux was to run APEX in autodetection mode on the newly created mosaics. This task masks preliminary bright sources to measure the background, then measures background subtracted fluxes in several fixed apertures (1", 3", and 5"). Sources found to be a specified level (in our case 3σ) above the background have their aperture fluxes summed and output in $\mu\text{Jy}/\text{sr}$. After autodetections were compiled into a MIPS catalog, they were matched to the R -band sources of the WFI source catalog within a search radius of 1" (shifts and rotations of the two catalogs relative to each other were negligible). This resulted in ~ 2100 matches.

APEX also allows for forced aperture photometry at fixed positions. For every galaxy location

Table 2.1: MIPS $24\mu m$ Scans

<i>PointingID</i> (a)	<i>N_{scans}</i> (b)	<i>FluxLimit</i> (c)
cl1040.7-1155	2	132
cl1054.4-1146	2	130
cl1054.7-1245	2	123
cl1216.8-1201	3	130
cl1232.5-1250	1	343
cl1227.9-1138	1	224
cl1354.2-1230	3	108

(a) The EDisCS cluster designation for the MIPS pointing. (b) The number of scans combined to create the final image. (c) The flux limit in μJy corresponding to $S/N = 3$ of each field of view.

derived from the R -band images, we measured 3 aperture fluxes on the MIPS image. The flux measurement from APEX is accompanied by a S/N estimate and we use those galaxies with $S/N \geq 3$ as MIPS sources in subsequent analysis. A listing of these flux limits is given in Table 2.1.

2.4.3 Conversion to Star Formation Rate

We used $24\mu m$ fluxes to estimate the total infrared luminosity (L_{IR}), which in turn is converted to a SFR. Dale & Helou (2002) describes the process by which a single measurement (namely $24\mu m$) can be extrapolated to the entire spectral energy distribution (SED) at IR wavelengths ($8 < \frac{\lambda}{\mu m} < 1000$) by way of model SED fitting. We fit rest-frame SEDs from Chary & Elbaz (2001) to the observed $24\mu m$ flux and spectroscopic redshifts. Once the IR SED is obtained, we integrate over the appropriate wavelength range and estimate the total L_{IR} . Using the prescription of Kennicutt (1998), we convert the total L_{IR} into an instantaneous SFR as

$$SFR(M_{\odot}year^{-1}) = 4.5 \times 10^{-44} L_{IR}(ergs s^{-1})$$

where L_{IR} is the total infrared luminosity integrated over 8–1000 μm . We use the flux limits derived in §2.4.2 to derive the SFR limit at each cluster redshift. These limits are presented in Table 2.2.

2.4.4 MIPS Stacking

In order to probe star formation rates beyond those derived from the $S/N \geq 3$ flux limits of our MIPS sources, a stacking method of all R -band selected galaxies (even those with MIPS flux $S/N < 3$) is implemented. To ensure that the flux of the stacked MIPS image is not biased to lower values, passive galaxies must first be identified and removed from the pool of non-detected galaxies. We use a UVJ diagram to do this. Figure 2.7 shows all cluster members on the UVJ diagram. All galaxies that fall in the upper left region defined by Williams et al. (2009) are classified as passive. The rest of the galaxies in the UVJ diagram are deemed to be star forming. We create a median stack of these galaxies by isolating thumbnail cut outs of the MIPS image centered around the location of these galaxies as determined by the R -band detections of each target. The IRAF routine imshift, which conserves flux during pixel interpolations, was used to center each galaxy within these 31x31 cutouts. A pixel by pixel median was then computed to produce the median

Table 2.2: MIPS derived Limits

ID(a)	L_{IR} Limit(b)	SFR limit(c)	$N_{MIPSmembers}$ (d)	$N_{MIPSfieldgalaxies}$ (e)
cl1040.7-1155	9.136e+10	15.73	7	55
cl1054.4-1146	9.25e+10	15.93	5	35
cl1054.7-1245	8.60e+10	14.79	17	42
cl1216.8-1201	1.11e+11	19.05	11	20
cl1232.5-1250	1.42e+11	24.42	3	12
cl1227.9-1138	1.34e+11	23.01	1	12
cl1227.9-1138a	1.22e+11	20.96	4	12
cl1354.2-1230	8.19e+10	14.10	10	17
cl1354.2-1230a	5.49e+10	9.45	10	20

aThe EDisCS cluster designation for the MIPS pointing. bThe Infrared Luminosity Limit L_{sol} . cStar Formation Rate limit in $M_{sol}/Year$. dNumber of member galaxies above the SFR limit. eNumber of non-member galaxies above the SFR limit and with the redshift range, $0.5 < z < 0.8$.

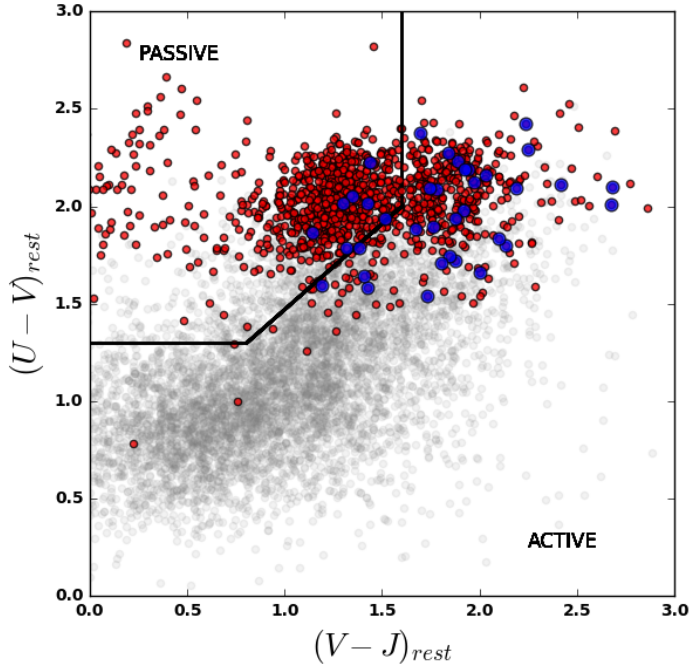


Figure 2.7: This is a plot of the rest frame U-V, V-J colors. The upper left hand corner defines the subset of galaxies deemed as passive to be excluded from the MIPS stacking exercise. Open circles are everything with UVJ colors in the redshift range $0.5 \leq z \leq 0.8$. Blue and red filled circles are mass complete cluster members above and below the SFR limit respectively.

stacked thumbnail. The uncertainty images were manipulated in a similar way, and the thumbnails of the uncertainties were stacked in quadrature. These were used when aperture photometry was performed at the center of each thumbnail. To further characterize the uncertainty of the stacks, 500 bootstrap iterations of each stack were created using a random subset of each stack's constituent thumbnails.

2.5 Sample Selection

In total, 9 clusters within $0.52 < z < 0.81$ and 1 corresponding field sample have been generated from our self contained data set. Classification of field and cluster members, as well as the construction of an aggregate cluster population will be discussed in the following sections.

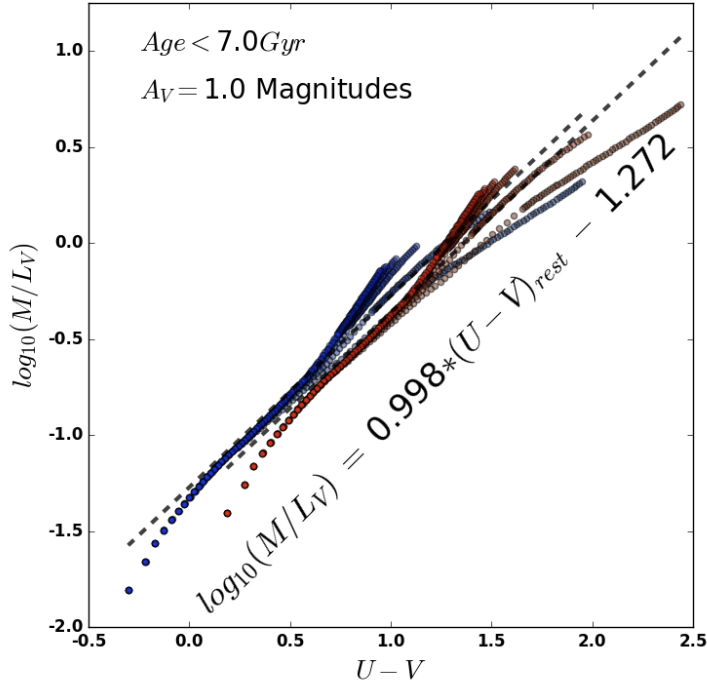


Figure 2.8: The blue and red points show the M/L_V ratio vs $U - V$ color relationship for 6 exponentially decaying star formation histories ($t_0 = [1, 2, 4, 6, 8, 10]$) produced by EZGal with Chabrier IMFs and Bruzual Charlot SPS models. The red points are created by adding an attenuation factor of 1 to the V -band magnitudes. Ages of the stellar populations are limited to 7Gyr .

2.5.1 Stellar Mass and Completeness

Due to the range of redshifts spanned by the EDisCS clusters, magnitude limits and hence stellar mass limits must be calculated for each cluster individually. Using EZGal (Mancone & Gonzalez (2012)), several Bruzual and Charlot stellar population synthesis (SPS) models with exponentially decaying ($t_0 = 1, 2, 4, 6, 8, 10 \text{ Gyr}$) star formation rates and Chabrier initial mass functions (IMFs) were compiled. By convolving the SPS models with the same filters used in the UVJ diagram, we can deduce a relationship between the rest-frame $U - V$ color and the mass to light ratio in the rest frame V -band (M/L_V). Figure 2.8 shows the direct relationship between rest frame $U - V$ color and the M/L_V ratio calculated with EZGal. The affect of dust on this relationship is shown as the red points in Figure 2.8, where we apply an attenuation of 1 to the V -band before plotting the

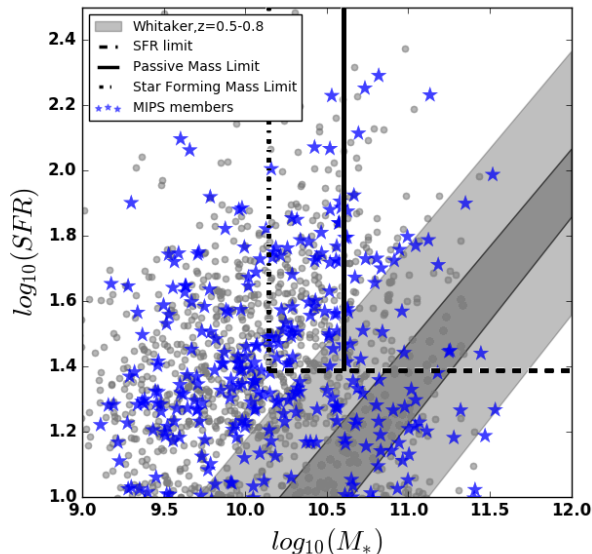


Figure 2.9: MIPS derived SFRs vs $\log_{10}(M_*)$. Grey points are all galaxies in the sample within a range of $0.5 < z < 0.8$ with a mass and SFR measurement. Blue stars are spectroscopic cluster member galaxies with MIPS detections. The grey horizontal dashed line indicates the SFR limit. The dash-dot and solid vertical lines demark the mass limits for star forming and passive galaxies respectively. The shaded grey region is the star forming main sequence as measured in Whitaker et al. (2012).

relationship. We use the line fit to the unattenuated blue points in Figure 2.8 to calculate the M/L_V for our galaxies. This ratio in conjunction with the V -band luminosity gives us stellar masses for our sample.

The completeness limit for these masses is calculated assuming the distribution M/L_V has no dependence on the total L_V . We take the brightest V -band clusters and shift their magnitudes down to the V -band magnitude limit. In doing so, the distribution of galaxy M/L_V ratios is also shifted downward. We calculated a L_V conversion factor based on the magnitude difference between the magnitude limit and the galaxy's magnitude. Once all the galaxy masses are calculated with this shifted L_V and the M/L_V calculated with EZGal, the mass limit is set to be that which includes 80% of the galaxies. This limit is $\log(M_\odot) \geq 10.6$ and $\log(M_\odot) \geq 10.14$ for passive and star forming galaxies, respectively. A star forming main sequence of our sample and comparison to the literature is given in Figure 2.9.

2.5.2 Defining Cluster Membership

In order to limit the amount of contamination due to superposition affects, multiple spectroscopic surveys were undertaken: FORS, Hectospec, and LDP. The given listing is also a rank ordering of the precision of each survey. Although the combination of these surveys does introduce some inhomogeneity within our sample, the spectra are only used for the determination of redshifts. In the case where a galaxy might have multiple spectroscopic measurements, a decision tree based on the aforementioned rank ordering of reliability is employed to pick the most appropriate redshift calculation to use. A FORS spectra is always used when present, then Hectospec, and lastly an LDP redshift is used. The difference in handling of the redshift measurements occurs when determining the redshift slice around a cluster's redshift to use in the determination of membership. A cluster's redshift, z_{clus} , is determined by that of its BCG. A galaxy's redshift, z_{gal} , from FORS or Hectospec is treated the same and these galaxies are considered members if their corresponding recession velocity, $\frac{c}{1+z_{gal}}$, is within $\pm 3\sigma$ of the cluster's recession velocity, $\frac{c}{1+z_{clus}}$ (σ being the cluster's velocity dispersion). LDP galaxies are considered members when the difference between z_{gal} and z_{clus} is less than 0.02. The difference in handling of these redshift solutions stems from the quality of the data. The Hectospec and FORS redshifts are precise enough for a direct comparison of the galaxy and cluster velocity dispersions, whereas the LDP redshifts are limited by their precision in z space. We use a 3σ cut on the LDP redshifts, where σ is the standard deviation of the difference between the high quality LDP and FORS redshifts ($\sigma \sim 0.004$ for the galaxies compared in Just et al. (2019)).

2.5.3 Aggregate Cluster Sample

To combat low number statistics of individual clusters, we create a composite cluster containing all cluster members (232 mass complete galaxies). After normalizing the clustercentric radius of each galaxy by the R_{200} of its host cluster, we stack them in catalog space into one composite structure. The composite cluster approximates spherical symmetry much more closely than any individual cluster can, and in so doing, justifies the use of a single parameter (clustercentric radius) to look at

SFR as a function of environment.

2.5.4 Defining Field Sample

Our field sample is created by using all galaxies within the redshift range of $0.5 < z < 0.8$ that are not flagged as cluster members and are brighter than 22.6 magnitudes in the R -band (the magnitude limit of the original EDisCS photometry). Because average star formation rates depend on stellar mass and redshift, we match our field and cluster samples in both of these quantities. Figure 2.10 shows both the redshift and mass dimensions of this matching process. For each cluster member's mass and redshift, a subset of field galaxies were chosen to be within 0.2 dex in mass and 0.05 in redshift. We chose one field galaxy at random from this phase space near neighbor subset to be added to the mass and redshift matched field sample.

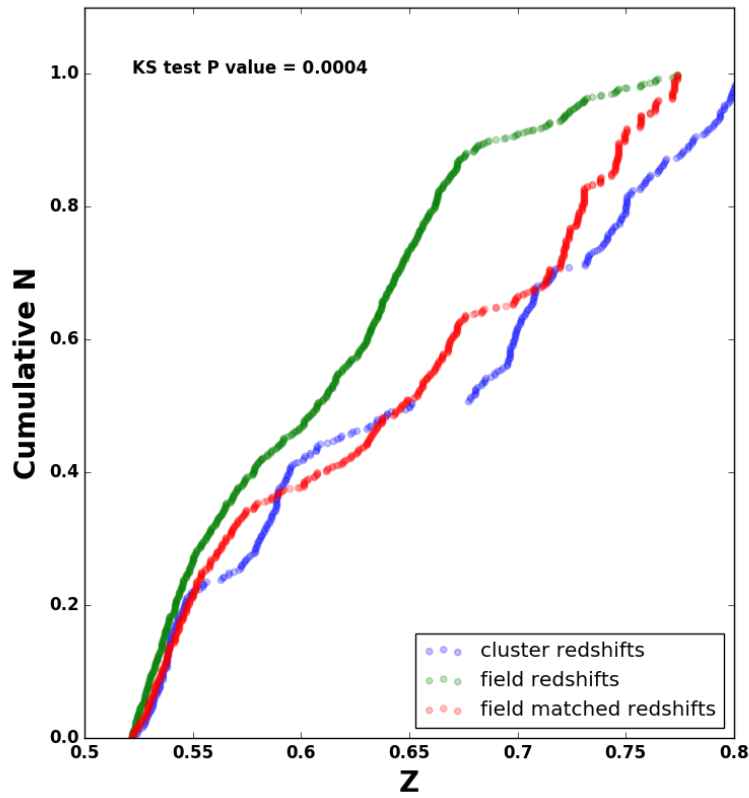
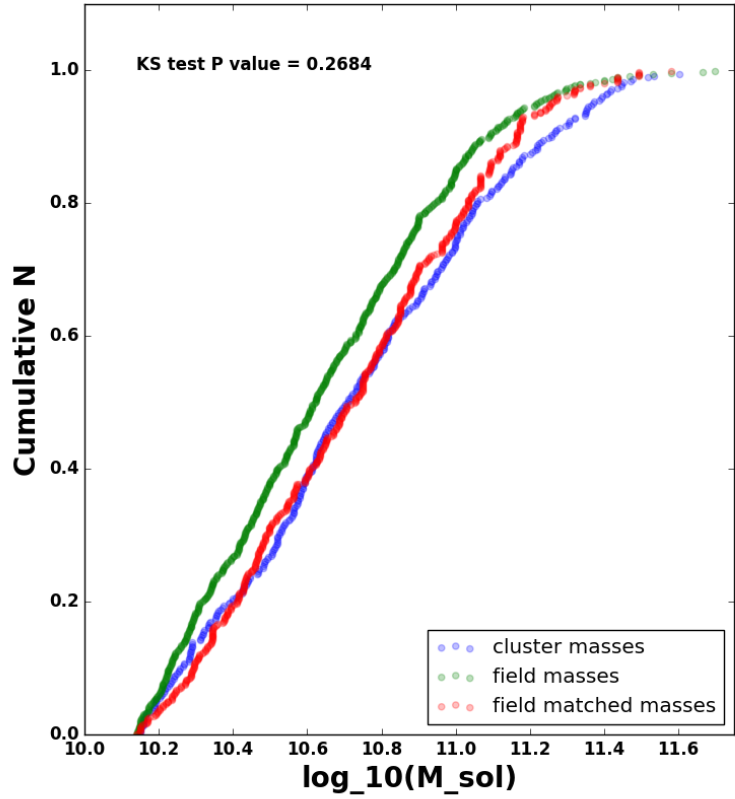


Figure 2.10: The cumulative distributions of the field (green points), the clusters (blue points), and the redshift/stellar mass matched field (red points). The redshift and mass distributions of the field were simultaneously matched to those of the clusters.

Chapter 3

Results

The following sections will show the relationship between the fraction of star forming galaxies and the average SFR as functions of clustercentric radius. We utilize two different mass limits in these analysis. For the fraction of star forming galaxies, we use the mass limit of passive galaxies ($\log(M_*) \geq 10.6$) and the highest 3σ SFR limit of the cluster sample ($SFR \geq 24.4M_\odot/\text{yr}$). Because the average SFR analysis uses only *UVJ* selected SF galaxies in the IR image stacking process, we use the lower mass limit of $\log(M_*) \geq 10.14$ that is obtained by excluding passive galaxies in the calculation.

3.1 Star Forming Fraction

Firstly, we investigate the fraction of MIPS sources in clustercentric radial bins of R_{200} . Figure 3.1 shows these MIPS fractions. The low number statistics per bin add significantly to the binomial errors of each fraction. Hence, two additional fractions (red points in Figure 3.1) were calculated using the total numbers found inside and outside $2 * R_{200}$. This division point is arbitrary, but it is the location where the fraction of backplash galaxies rises to $\sim 50\%$. For galaxies outside of $2 * R_{200}$, the field and cluster fractions are indiscriminable. Inside this radius, the cluster shows a 40% reduction relative to the field fractions. We apply the current mass and SFR limits to the data presented in Finn et al. (2010), which yields the MIPS fractions shown by the gray squares in Figure 3.1. It is noted that the star forming fractions of this work and those of Finn et al. (2010) are consistent. Together, these data show that the MIPS fraction within clusters does not reach field values until a radial distance of at least $2 * R_{200}$.

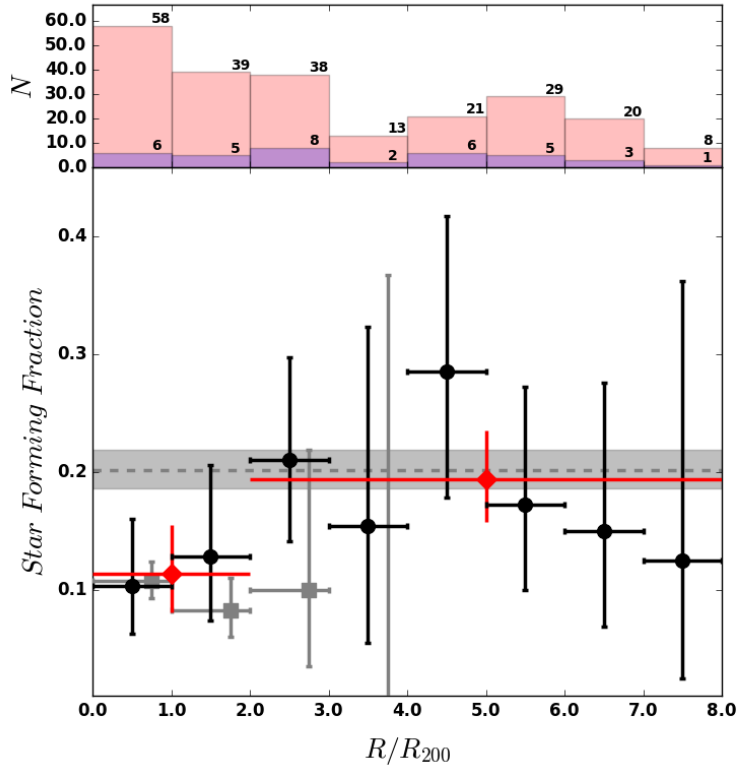


Figure 3.1: The histogram on top shows bin totals in red and SF totals in blue. These totals are summed over all clusters with galaxies above the mass complete limit. The lower panel shows fractions of SF galaxies in bins of R_{200} as the black points. Binomial limits for the SF fractions are given for each radial bin. Red points are the fractions calculated in two coarse bins, inside and outside of $2R_{200}$. Grey points are the star forming fractions from Finn et al. (2010) calculated with the mass and SFR limits from this study applied.

3.2 Average Star Formation

Because of the shallow nature of our MIPS $24\mu m$ data, we are unable to probe below the star forming main sequence at our redshift range. To mitigate this shortcoming, forced photometry was applied to the MIPS images at all locations determined by detections in the R -band images that correspond to UVJ selected star formers. Using the techniques of Williams et al. (2009) we are able to sufficiently divide our sample into two groups, star-forming and passive, by parsing the $U - V$ vs $V - J$ color space appropriately (see Figure 2.7). All galaxies above the passive mass completeness limit that are classified as star-formers in the UVJ diagram were median stacked as a

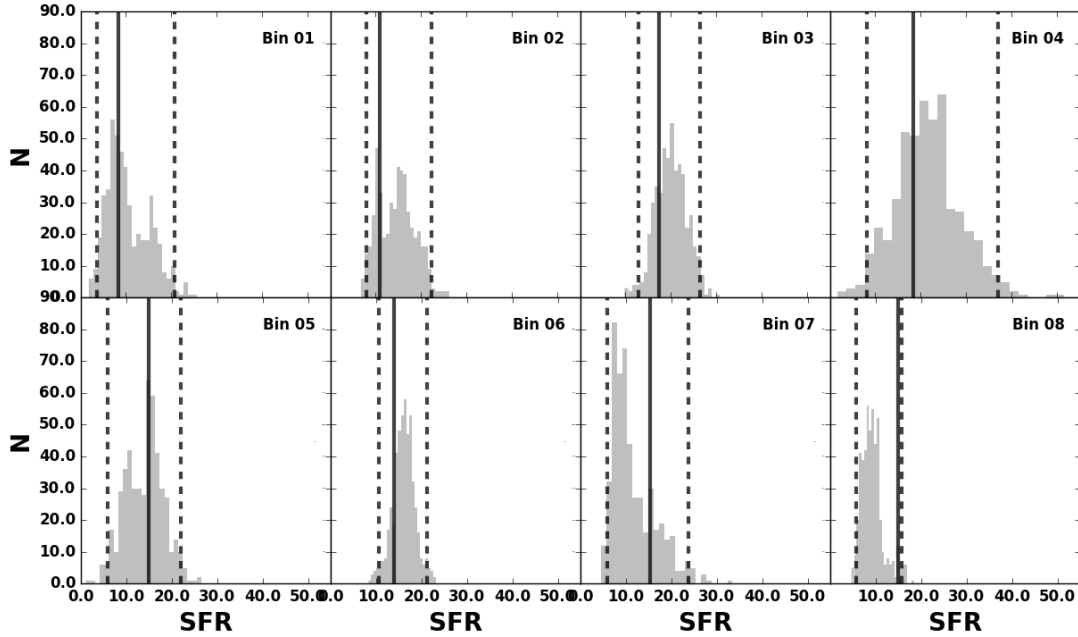


Figure 3.2: These are histograms of the SFR measured from 500 bootstrap iterations of the MIPS stack for each radial bin of our composite cluster. The solid black line is the SFR measure from the original stack and the dashed black lines indicate the 95 percentile region of the bootstrap iterations.

composite source. The benefits of stacking MIPS fluxes are shown in a number of studies of faint sources (Zheng et al., 2006, 2007; Dole et al., 2006; Dye et al., 2007). The flux measured on this median image yields an average star formation rate for star forming galaxies. By doing this we can begin to probe below our individual detection limit and measure the mean SFR of star forming galaxies. Figure 3.2 shows the distribution of SFRs derived from the 500 bootstrap iterations that we make for each composite cluster radial bin. The 95 percentile ranges of these distributions are used for the uncertainties shown in Figure 3.3, which displays the SFRs calculated from the median MIPS images of cluster members as a function of R/R_{200} . The gray bar in Figure 3.3 indicates the average SFR of all field galaxies stacked in the same manner. The consistency of cluster member and field galaxy average SFRs is noted and will be reviewed in the discussion.

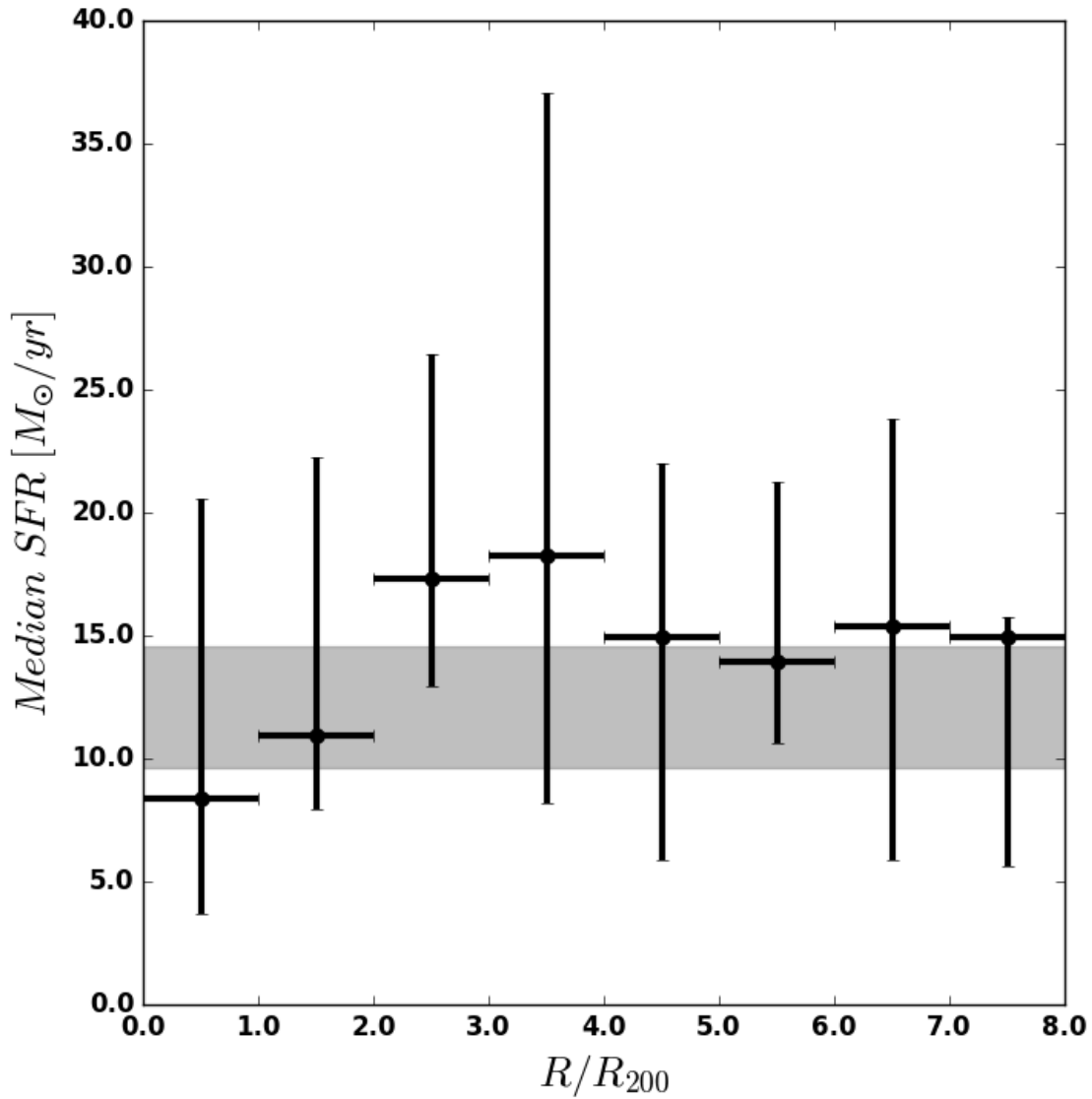


Figure 3.3: Average SFRs measured from stacked MIPS images of UVJ selected star forming galaxies. Error bars derived from the 95 percentile of 500 bootstrap iterations of each stack. Black cross hairs indicate cluster members with the specified radial bin. Gray bar represents the average SFR of field galaxies.

Chapter 4

Discussion

As noted in the results section, the fraction of SF galaxies remains consistent with field at large radii, with a nominal drop only at the very central region of the composite cluster. Given the errorbars of our SF fractions, we can rule out all SFR declines from the field value that are greater than 1.7. This means that we find a 40% decrease of the star forming fraction in the cluster relative to the field value. In addition to this decrease in the fraction of SF galaxies, we see that the average SFR of the cluster galaxies is consistent with the field at all radii.

One explanation that can rectify these two facts simultaneously, is that of quickly truncated star formation in cluster galaxies. For sufficiently quick timescales of suppression, you would not expect to see a drop in the average SFR with respect to the field because the galaxies undergoing the star formation truncation process would not occupy intermediate SFR values for very long. Hence, for any decrease in cluster star forming fractions, you would not expect to see a decrease of the average SFR.

Chapter 5

Summary

This paper has added several new data sets to the ESO Distant Cluster Survey collaboration. I reduced UKIRT *K*-band images and added fluxes to the EDisCS catalogs. I reduced spectroscopic data from Hectospec and added redshifts solutions for EDisCS galaxies. I reduced and added photometry to the EDisCS catalog for the MIPS $24\mu\text{m}$ data. These data, in conjunction with other EDisCS data, lead to two main results: the fraction of star forming galaxies shows a nominal reduction only in cluster cores and the average star formation rate of these galaxies is independent of clustercentric radius.

References

- Balogh, M. L., Baldry, I. K., Nichol, R., et al. 2004, , 615, L101
- Balogh, M. L., Schade, D., Morris, S. L., et al. 1998, , 504, L75
- Bell, E. F., & de Jong, R. S. 2001, , 550, 212
- Blanton, M. R., & Moustakas, J. 2009, , 47, 159
- Chary, R., & Elbaz, D. 2001, , 556, 562
- Clowe, D., Schneider, P., Aragón-Salamanca, A., et al. 2006, , 451, 395
- Currie, M. J., Berry, D. S., Jenness, T., et al. 2014, in *Astronomical Society of the Pacific Conference Series*, Vol. 485, *Astronomical Data Analysis Software and Systems XXIII*, ed. N. Manset & P. Forshay, 391
- Dale, D. A., & Helou, G. 2002, , 576, 159
- Dole, H., Lagache, G., Puget, J.-L., et al. 2006, , 451, 417
- Dwek, E., & Arendt, R. G. 1998, , 508, L9
- Dye, S., Eales, S. A., Ashby, M. L. N., et al. 2007, , 375, 725
- Fabricant, D., Fata, R., Roll, J., et al. 2005, , 117, 1411
- Finn, R. A., Desai, V., Rudnick, G., et al. 2010, , 720, 87
- Fixsen, D. J., Dwek, E., Mather, J. C., Bennett, C. L., & Shafer, R. A. 1998, , 508, 123
- Gómez, P. L., Nichol, R. C., Miller, C. J., et al. 2003, , 584, 210

Gonzalez, A. H., Zaritsky, D., Dalcanton, J. J., & Nelson, A. 2001, , 137, 117

Gorjian, V., Wright, E. L., & Chary, R. R. 2000, , 536, 550

Gunn, J. E., & Gott, III, J. R. 1972, , 176, 1

Hashimoto, Y., Oemler, Jr., A., Lin, H., & Tucker, D. L. 1998, , 499, 589

Hauser, M. G., Arendt, R. G., Kelsall, T., et al. 1998, , 508, 25

Hernquist, L., & Mihos, J. C. 1995, , 448, 41

Hogg, D. W., Blanton, M. R., Brinchmann, J., et al. 2004, , 601, L29

Just, D. W., Kirby, M., Zaritsky, D., et al. 2019, , 885, 6

Kauffmann, G., White, S. D. M., Heckman, T. M., et al. 2004, , 353, 713

Kennicutt, Jr., R. C. 1998, , 36, 189

Lagache, G., Abergel, A., Boulanger, F., Désert, F. X., & Puget, J.-L. 1999, , 344, 322

Larson, R. B., Tinsley, B. M., & Caldwell, C. N. 1980, , 237, 692

Lewis, I., Balogh, M., De Propris, R., et al. 2002, , 334, 673

Lonsdale, C. J., Smith, H. E., Rowan-Robinson, M., et al. 2003, , 115, 897

Mancone, C. L., & Gonzalez, A. H. 2012, Publications of the Astronomical Society of the Pacific,
124, 606

McGee, S. L., Balogh, M. L., Bower, R. G., Font, A. S., & McCarthy, I. G. 2009, , 400, 937

Moore, B., Katz, N., Lake, G., Dressler, A., & Oemler, A. 1996, , 379, 613

Papovich, C., Cool, R., Eisenstein, D., et al. 2006, , 132, 231

Peng, Y.-j., Lilly, S. J., Kovač, K., et al. 2010, , 721, 193

Poggianti, B. M., von der Linden, A., De Lucia, G., et al. 2006, , 642, 188

Puget, J.-L., Abergel, A., Bernard, J.-P., et al. 1996, , 308, L5

Rieke, G. H., Young, E. T., Engelbracht, C. W., et al. 2004, , 154, 25

Schlegel, D. J., Finkbeiner, D. P., & Davis, M. 1998, , 500, 525

Vulcani, B., Poggianti, B. M., Finn, R. A., et al. 2010, , 710, L1

Whitaker, K. E., van Dokkum, P. G., Brammer, G., & Franx, M. 2012, , 754, L29

White, S. D. M., Clowe, D. I., Simard, L., et al. 2005, , 444, 365

Williams, R. J., Quadri, R. F., Franx, M., van Dokkum, P., & Labbé, I. 2009, , 691, 1879

Wright, E. L. 2001, , 553, 538

Wright, E. L., & Reese, E. D. 2000, , 545, 43

Zheng, X. Z., Bell, E. F., Rix, H.-W., et al. 2006, , 640, 784

Zheng, X. Z., Dole, H., Bell, E. F., et al. 2007, , 670, 301

Chapter 6

Appendix

